Metal-Insulator Transition of Dirac Fermions: Variational Cluster Study

Masaki Ebato, Tatsuya Kaneko, and Yukinori Ohta

Department of Physics, Chiba University, Chiba 263-8522, Japan

A comparative study is made on the metal-insulator transition of Dirac fermions in the honeycomb and π-flux Hubbard models at half filling by means of the variational cluster approximation and cluster dynamical impurity approximation. Paying particular attention to the choice of the geometry of solver clusters and the inclusion of particle-bath sites, we show that the direct transition from the Dirac semimetallic state to the antiferromagnetic Mott insulator state occurs in these models, and therefore, the spin liquid phase is absent in the intermediate region, in agreement with recent quantum-Monte-Carlo–based calculations.

1. Introduction

The mechanism of the metal-insulator transition (MIT) has long been one of the central issues in strongly correlated electron systems.[1,2] In particular, the MIT in correlated Dirac fermion systems has attracted much attention recently, a typical example of which is the honeycomb-lattice Hubbard model at half filling representing graphene.[3] Because the honeycomb lattice is bipartite and free from frustration, the Néel antiferromagnetic (AF) Mott insulator (MI) state is realized in the strong coupling region. However, unlike in the square-lattice Hubbard model, where perfect Fermi surface nesting is present, one expects that the AF order will not appear in the weak coupling region but rather the massless Dirac semimetallic (SM) state will be maintained until a critical interaction strength is reached.[4–7]

The MIT in the honeycomb lattice was studied by Meng *et al.*[8] using the quantum Monte Carlo (QMC) method, whereby they claimed the presence of a quantum spin liquid (SL) state (or nonmagnetic MI state) in the intermediate region between the Dirac SM state and the antiferromagnetic Mott insulator (AFMI) state. Their study attracted much interest because it suggested the emergence of the SL state in systems without frustration in their spin degrees of freedom. However, subsequent studies based on the large-scale QMC method,[9] the pinning field approach using the QMC method,[10] and analysis of the quantum criticality by finite-size scaling[10,11] have consistently suggested the direct transition from the SM state to the AFMI state, and therefore we now anticipate that the SL state is absent in this model. Similar debates have also been had for the π-flux Hubbard model, another Dirac fermion system, whereby the direct transition from the SM state to the AFMI state is now anticipated.[11–13]

Quantum cluster methods have also been used to study the MIT in the honeycomb Hubbard model.[14–24] In particular, cluster dynamical mean-field theory (CDMFT) and variational cluster approximation (VCA) calculations have shown that if the 6-site hexagonal ring is used as a solver cluster, the single-particle band gap opens even in the weak coupling region where the AF order is absent, thereby suggesting the presence of the SL state.[17–20] However, the opening of the band gap at the infinitesimal interaction strength was questioned,[19–21] and moreover, from comparison with the results of the cluster dynamical impurity approximation (CDIA) and dynamical cluster approximation (DCA), the emergence of the nonmagnetic insulator phase predicted by the CDMFT and VCA was considered to be unrealistic.[21–24] So far, not much is known about the MIT in the π-flux Hubbard model studied by quantum cluster methods.

In this paper, motivated by the above development in the field, we will make a comparative study on the MIT of correlated Dirac fermions in the honeycomb and π-flux Hubbard models at half filling by means of the VCA and CDIA. We will, in particular, point out that a suitable choice of the cluster geometry is essential in the quantum cluster calculations to suppress the opening of the band gap in the weak-coupling region and that the inclusion of particle-bath sites is important in discussing the order of the MIT as well as the transfer of spectral weight in the single-particle spectral function. We will thereby show that the direct transition from the Dirac SM state to the AFMI state occurs with increasing interaction strength in these models and that the SL phase is absent in their intermediate coupling region.

2. Models and Methods

The honeycomb and π-flux Hubbard models may be defined by the Hamiltonian

$$\mathcal{H} = -\sum_{i,j,\sigma} t_{ij} c^{\dagger}_{i\sigma} c_{j\sigma} + U \sum_{i} n_{i\uparrow} n_{i\downarrow}, \tag{1}$$

where $c^{\dagger}_{i\sigma}$ is the creation operator of a fermion (which will be referred to as an electron hereafter) with spin σ at site

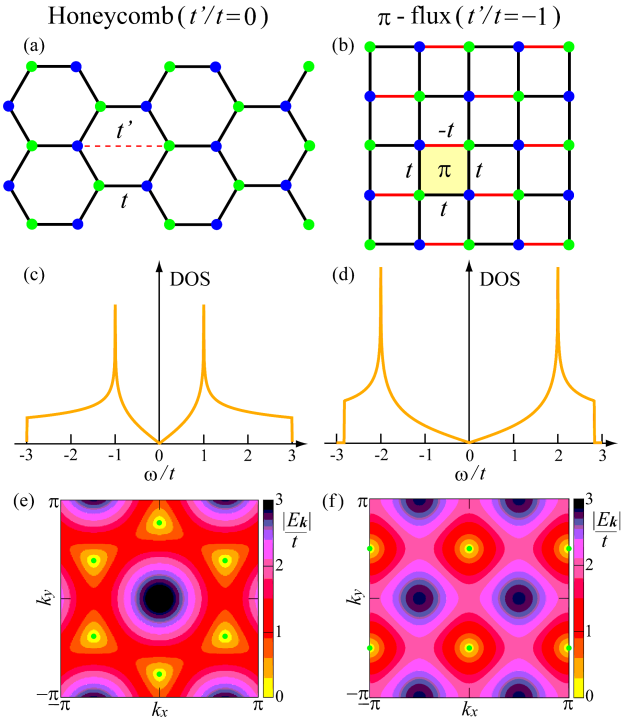

Fig. 1. (Color online) Schematic representations of the (a) honeycomb ($t'/t = 0$) and (b) π-flux ($t'/t = -1$) lattices. The dashed line in (a) indicates the bonds with the hopping parameter t' and the red lines in (b) indicate the bonds with the negative hopping parameter $t' = -t$. Noninteracting DOSs [(c) and (d)] and contour plots of the band dispersions $E_{\boldsymbol{k}}$ [(e) and (f)] are also shown for the honeycomb (left panels) and π-flux (right panels) lattices. The green dots in (e) and (f) indicate the Dirac points in $\boldsymbol{k}$-space.

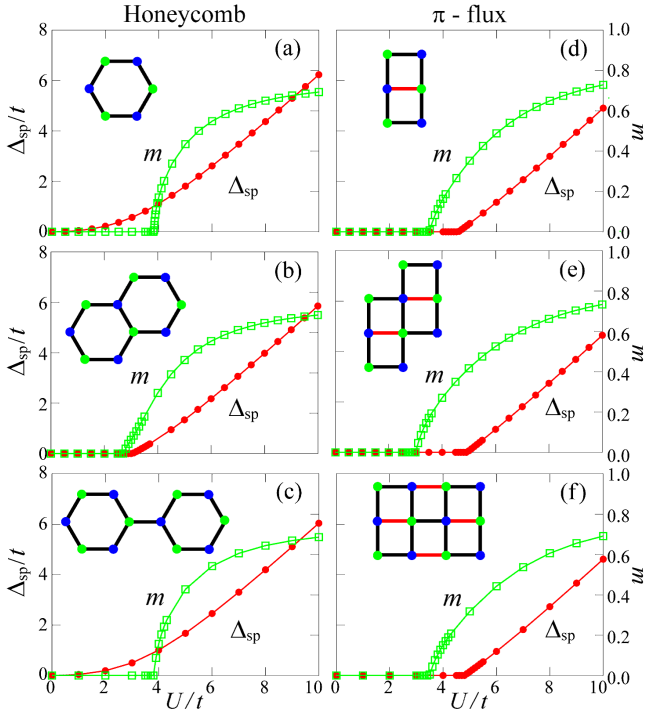

Fig. 2. (Color online) Single-particle gap $\Delta_{\rm sp}$ in the PM state and local magnetization m in the AF state calculated by the VCA as functions of U/t. The results for the honeycomb Hubbard model are shown in (a), (b), and (c) and those for the π-flux Hubbard model are shown in (d), (e), and (f). The geometry of the solver cluster used is illustrated in each panel.

i and $n_{i\sigma} = c^\dagger_{i\sigma} c_{i\sigma}$. t_{ij} is the hopping amplitude: we define $t_{ij} = t$ for the nearest-neighbor bonds and $t_{i,j} = t'$ for the bonds connecting hexagons in the honeycomb lattice [see Fig. 1(a)]. U is the on-site Coulomb repulsion. We assume the filling of one electron per site (half filling). Changing the value of t', we can tune the system continuously from the honeycomb lattice at $t' = 0$ to the π-flux lattice at $t' = -t$ [see Fig. 1(b)].[25] At $U = 0$, these systems at low energies are described in terms of the massless Dirac fermions; their densities of states (DOSs) and band dispersions are shown in Figs. 1(c)-1(f).

We apply the VCA,[26–28] which is a quantum cluster method based on self-energy functional theory (SFT).[29,30] In the VCA, we introduce disconnected finite-size clusters (that are solved exactly) as a reference system. By restricting the trial self-energy to the self-energy of the reference system Σ', we can obtain the grand potential of the original system in the thermodynamic limit as

$$\Omega = \Omega' + \mathrm{Tr}\ln(G_0^{-1} - \Sigma')^{-1} - \mathrm{Tr}\ln(G'), \qquad (2)$$

where Ω', G', and G_0 are the grand potential, the Green's function of the reference system, and the noninteracting Green's function, respectively. The short-range correlations within the cluster of the reference system are taken into account exactly. The one-body parameters $\boldsymbol{t}'$ of the reference system are optimized according to the variational principle $\partial\Omega[\Sigma'(\boldsymbol{t}')]/\partial\boldsymbol{t}' = 0$. In the VCA, we can treat the spontaneous symmetry breaking by adding appropriate Weiss fields to the reference system.[31] We have to choose an exactly solvable reference system; here we apply an exact diagonalization method and solve the quantum many-body problem in the cluster of the reference system.

We also use the CDIA,[32] which is an extended version of the VCA where particle-bath sites are added to the clusters to take into account the electron-number fluctuations in the correlation sites. In the CDIA, we optimize the hybridization parameter between the bath and correlation sites V and the on-site energy of the bath sites ε based on SFT.[32,33] Note that the CDIA is intrinsically equivalent to CDMFT with an exact-diagonalization solver.

3. Results and Discussion

3.1 Results of VCA

First, let us consider the single-particle gap $\Delta_{\rm sp}$ in the paramagnetic (PM) state and the staggered mag-

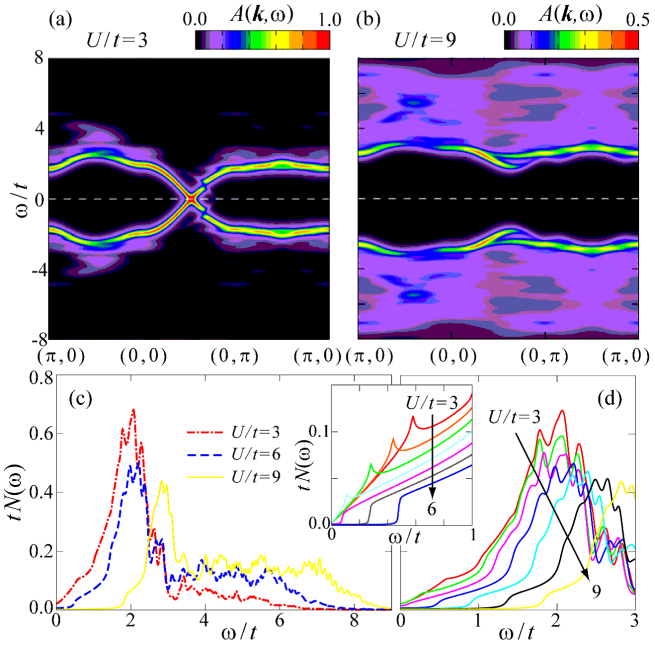

Fig. 3. (Color online) Single-particle spectral function $A(\boldsymbol{k},\omega)$ [(a) and (b)] and DOS $N(\omega)$ [(c) and (d)] in the PM states of the π-flux Hubbard model calculated by the VCA with the 12-site cluster. The horizontal dashed line in (a) and (b) indicates the Fermi level. We applied the artificial Lorentzian broadening of the spectra of $\eta/t = 0.15$ in (a) and (b) and $\eta/t = 0.05$ in (c) and (d). The inset in the lower panels is an enlargement of the DOS near the Fermi level, assuming $\eta/t = 0.005$.

netization m in the AF state, which are calculated for the honeycomb and π-flux Hubbard models using the VCA. We introduce the Weiss field associated with the two-sublattice Néel order and evaluate the local magnetization $m = \langle n_{i\uparrow} - n_{i\downarrow} \rangle$. The gap $\Delta_{\rm sp}$ is evaluated in the absence of the Weiss field as the jump of the chemical potential with respect to the number of electrons in the system. Note that the band gap always opens when the AF order appears. We use clusters of 6, 10, and 12 sites as reference systems; the clusters used for the honeycomb and π-flux lattices are topologically equivalent but with different hopping parameters (see Fig. 2).

The results for the honeycomb Hubbard model are shown in Figs. 2(a)-2(c). We find that the MIT is sensitive to the choice of the clusters, i.e., the results obtained using the clusters of 6 and 12 sites are qualitatively different from those in the case of 10 sites. The AF order appears at $U_{\rm AF}/t = 3.8$ for the clusters of 6 and 12 sites, the results of which are in good agreement with results of QMC simulations.[9,10] However, the gap $\Delta_{\rm sp}$ opens at infinitesimal U values and the SM phase appears only at $U = 0$, thus suggesting the presence of the PM insulator state at $0 < U < U_{\rm AF}$. Recent studies, however, have claimed that this gap cannot be regarded as the true Mott gap,[21,22] the details of which will be discussed below. For the cluster of 10 sites, on the other hand, the SM phase persists up to a large U value and the transition to the AF phase occurs directly from the SM phase. Here, the AF order appears at $U_{\rm AF}/t = 2.7$ and the gap $\Delta_{\rm sp}$ opens at $U_{\rm PM}/t = 3.0$, qualitatively consistent with the results of recent QMC simulations, where the direct transition from the Dirac SM phase to the AFMI phase was predicted.[9,10]

The results for the π-flux Hubbard model are shown in Figs. 2(d)-2(f). We find that the results obtained using the clusters of 6, 10, and 12 sites are qualitatively the same as each other, i.e., the SM phase persists up to a large U value. The AF order appears at $U_{\rm AF}/t = 3.4$, 2.9, and 3.4 and the gap $\Delta_{\rm sp}$ opens at $U_{\rm PM}/t = 4.5$, 4.9, and 4.8 for the clusters of 6, 10, and 12 sites, respectively. Therefore, the PM insulator state does not exist between the SM and AFMI phases, in accordance with the results of recent QMC simulations that show the direct transition from the SM phase to the AFMI phase.[11,13] Note that the transition point $U_{\rm AF}$ of our VCA calculations is smaller than that of the QMC simulations, $U_{\rm AF}/t = 5.25$–5.5,[13] which may be due to the anisotropy of the clusters used in our calculations; the agreement becomes good if we use an isotropic cluster of 4 sites, which gives the value $U_{\rm AF}/t = 5.0$.

We also calculate the single-particle spectral function and DOS using cluster perturbation theory (CPT)[34] for the PM state of the π-flux Hubbard model. The results are shown in Fig. 3. We immediately find that the Dirac linear band dispersion is clearly visible near the Fermi level at $U < U_{\rm PM}$ [see Fig. 3(a)], whereas the band gap opens at $U > U_{\rm PM}$ [see Fig. 3(b)]. The transfer of spectral weight occurring with increasing U/t is seen in Figs. 3(c) and 3(d), which is characteristic of the VCA and will be discussed below in Sect. 3.2 in comparison with the results of the CDIA.

3.2 Results of CDIA

Next, let us discuss the roles of bath sites in MIT using the CDIA. Following a previous study on the honeycomb Hubbard model,[21] we examine the honeycomb and π-flux Hubbard models using the 4-site 6-bath cluster. The results are shown in Fig. 4. We find that the grand potentials of the honeycomb and π-flux Hubbard models both have two stationary points around the transition point U_c. The SM solution exists at a small U, which vanishes at U_{c2} with increasing U. The MI solution exists at a large U, which vanishes at U_{c1} with decreasing U. The two solutions thus coexist in the region $U_{c1} \le U \le U_{c2}$, and the ground-state energies cross at U_c. We obtain the values $U_{c1}/t = 6.6$, $U_{c2}/t = 7.7$, and $U_c/t = 7.5$ for the honeycomb Hubbard model and $U_{c1}/t = 8.6$, $U_{c2}/t = 10.3$, and $U_c/t = 9.8$ for the π-flux Hubbard model. The calculated result for $\Delta_{\rm sp}$ [see Figs. 4(c) and 4(d)] shows hysteresis between the SM ($\Delta_{\rm sp} = 0$) and MI ($\Delta_{\rm sp} > 0$) solutions, which indicates that $\Delta_{\rm sp}$ jumps dis-

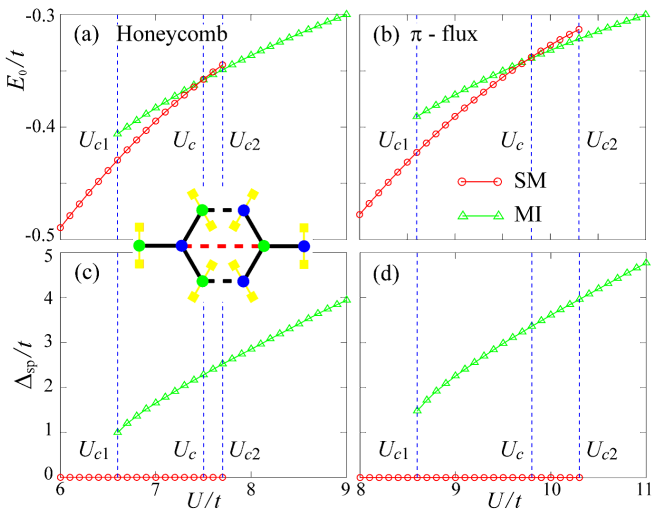

Fig. 4. (Color online) Ground-state energies [(a) and (b)] and single-particle gaps [(c) and (d)] in the PM state of the honeycomb and π-flux Hubbard models calculated by the CDIA, where the 4-site 6-bath cluster shown in the left panels is used.

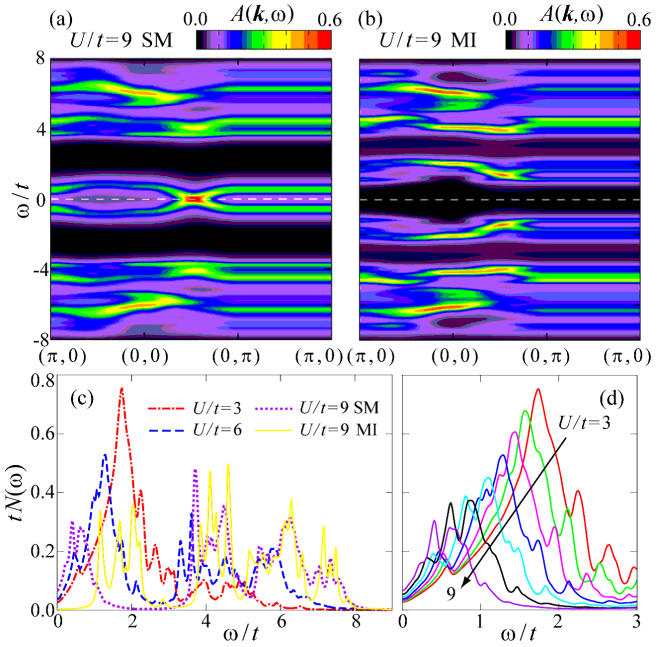

Fig. 5. (Color online) As in Fig. 3 but for the results of the CDIA with the 4-site 6-bath cluster. In (a)-(c), the single-particle spectral functions and DOSs of both the SM and MI states are shown at $U/t = 9$, while in (d), the DOS of only the SM state is shown.

continuously at U_c. These results clearly indicate that the MIT is of the first-order (or discontinuous) in the CDIA, which is in contrast to the results of the VCA where the second-order (or continuous) transition is found (see Fig. 2). The first-order MIT is thus expected in the actual honeycomb and π-flux Hubbard models in which the electron-number fluctuation is present.

To further clarify the roles of bath sites in the MIT, we examine the U dependence of the single-particle spectral function and the DOS calculated using CPT. The results for the π-flux Hubbard model obtained in the CDIA are shown in Fig. 5, where the Dirac linear band dispersion is clearly visible in the vicinity of the Fermi level. Note that the slope of the dispersion at the Dirac point becomes steeper for larger values of U.

Comparing the DOS curves, we find that the results in the VCA (see Fig. 3) are indeed significantly different from those in the CDIA (see Fig. 5) in the following respects. (i) The spectral weight with a large peak at $\omega/t = 2$ in the $U/t \to 0$ limit [see Fig. 1(d)] is partially transferred to a broad higher-energy region corresponding to the "upper Hubbard band" with increasing U/t, which is observed in both the VCA and CDIA. (ii) With increasing U, the remaining spectral weight at $\omega/t \simeq 2$ shifts to higher energies in the VCA [see Figs. 3(c) and 3(d)], while in the CDIA, it shifts rapidly to lower energies and simultaneously loses its weight [see Figs. 5(c) and 5(d)]. (iii) We thus have a large spectral weight at low energies ($\omega/t \lesssim 1$) in the CDIA, which is rather small in the VCA. The spectral weight characteristic of the massless Dirac SM dispersions can, however, be seen in the vicinity of the Fermi level in both the VCA and CDIA spectra. (iv) More quantitatively, a kink appears in the lowest-energy region of the DOS in the VCA (see the inset of the lower panels of Fig. 3), which shifts toward the Fermi level with increasing U. The DOS curve becomes steeper near the Fermi level (or the $\boldsymbol{k}$-linear dispersion becomes flatter at the Dirac point), renormalizing the Fermi velocity but keeping the electrons massless. No quasiparticle peak appears. At a critical U value, the kink disappears and simultaneously the gap begins to open gradually. In the CDIA, similar but stronger effects can be seen with increasing U/t in the lowest-energy region of the DOS, until the gap opens discontinuously at U_c [see Figs. 5(c) and 5(d)]. These low-energy behaviors in the CDIA are consistent with the results of the single-site DMFT for the honeycomb Hubbard model[6,7] and are expected to be realistic in the honeycomb and π-flux Hubbard models where the electron-number fluctuates.

3.3 Cluster geometry dependence

Finally, let us discuss the cluster geometry dependence of the single-particle gap $\Delta_{\rm sp}$ in the PM phase. In Figs. 6(a) and 6(b), we show the results of the 6-site 6-bath system for the honeycomb Hubbard model and of the 4-site 4-bath and 4-site 8-bath systems for the π-flux Hubbard model. In the honeycomb lattice, we find that even if we add the bath sites, the gap $\Delta_{\rm sp}$ opens at any infinitesimal U value when we use the 6-site hexagonal ring cluster as the reference system.[19–21] In the π-flux

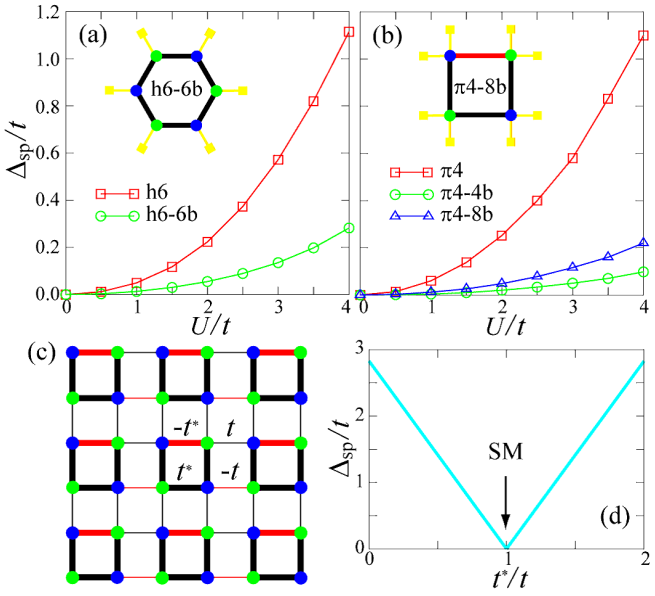

Fig. 6. (Color online) Calculated single-particle gap Δ_{sp} in the PM state of the (a) honeycomb and (b) π-flux Hubbard models. For the honeycomb lattice, we use the hexagonal 6-site cluster (h6) and 6-site 6-bath cluster (h6-6b). For the π-flux lattice, we use the square 4-site cluster (π4), 4-site 4-bath cluster (π4-4b), and 4-site 8-bath cluster (π4-8b). (c) π-flux lattice with renormalized hopping parameter t^* violating the original translational symmetry and (d) its noninteracting single-particle gap as a function of t^*/t.

Hubbard model, we also find that the gap Δ_{sp} opens at any infinitesimal U value when we use the 4-site square cluster as the reference system. Therefore, even though we use two bath sites per correlation site, the gap opens at infinitesimal U values, which does not agree with the argument in Ref. 21 that at least two bath sites per correlation site are necessary to discuss the MIT in the honeycomb lattice.

Rather, our results agree with the statement in Ref. 22 that the opening of the gap at infinitesimal U/t values is not caused by the bath degrees of freedom but by the cluster geometry, which violates the original translational symmetry of the lattice. We show the latter case in Fig. 6(c), where the original translational symmetry of the π-flux lattice is violated by the renormalization of the hopping parameter t^* by the interaction only within the cluster, leading to $t^* \neq t$. Then, as shown in Fig. 6(d), the noninteracting band with t^* and t has a finite single-particle gap unless $t^* = t$. A similar discussion has been given for the honeycomb lattice,[18,24] where the 6-site hexagonal clusters with the renormalized hopping parameter t^* are connected with the bare hopping parameter t. A "plaquette insulator" state is thus realized at $t^* \neq t$ in the noninteracting limit. This is the reason why the single-particle gap opens at infinitesimal U/t values. However, we here point out that it is always possible to make an appropriate choice of clusters that maintains the Dirac zero-gap situation even though it violates the original translational symmetry, examples of which are shown in Figs. 2(d)-2(f) where the gap does not open at small values of U. Thus, the statement in Ref. 22 is too strict. Careful choice of the clusters in the quantum cluster methods such as CDMFT, the VCA, and the CDIA enables one to discuss the MIT of Dirac fermion systems without spurious opening of the gap.

4. Summary

We have made a comparative study on the MIT of Dirac electrons in the honeycomb and π-flux Hubbard models using the VCA and CDIA, where we have calculated the single-particle gap and staggered magnetization as functions of the interaction strength U. We have paid particular attention to the choice of the cluster geometry and the inclusion of the bath sites. We have thus confirmed that the spurious single-particle gap that opens at infinitesimal U values is not caused by the bath degrees of freedom but rather by the cluster geometry. We have shown that with increasing U, the first-order MIT to the nonmagnetic MI phase occurs in the presence of electron-number fluctuation. However, the AFMI phase always preempts this MIT, at least in the present models, and therefore the SL phase previously suggested to emerge between the Dirac SM and AFMI phases is absent in these models.

Our results imply that, if the AF ordering can be suppressed by, for example, to the effect of spin frustrations in the triangular and related lattices, one may expect that the MI phase without AF orders will preempt the AFMI phase, resulting in the emergence of the SL phase in the intermediate coupling region, as was pointed out recently in Ref. 35 for the triangular π-flux Hubbard model.

We thank K. Seki for enlightening discussions. T. K. acknowledges support from a JSPS Research Fellowship for Young Scientists. This work was supported in part by KAKENHI Grant No. 26400349 from JSPS of Japan.

1) N. F. Mott, *Metal-Insulator Transitions*, (Taylor & Francis, London, 1990) 2nd ed.
2) M. Imada, A. Fujimori, and Y. Tokura, Rev. Mod. Phys. **70**, 1039 (1998).
3) Note that the honeycomb Hubbard model we use is not sufficient for a realistic description of graphene although it is the simplest for reproducing its Dirac-type electrons: see, for example, A. Castro Neto, F. Guinea, N. Peres, K. Novoselov, and A. Geim, Rev. Mod. Phys. **81**, 109 (2009); V. N. Kotov, B. Uchoa, V. M. Pereira, F. Guinea, and A. H. Castro Neto, Rev. Mod. Phys. **84**, 1067 (2012); M. Schüler, M. Rösner, T. O. Wehling, A. I. Lichtenstein, and M. I. Katsnelson, Phys. Rev. Lett. **111**, 036601 (2013).
4) S. Sorella and E. Tosatti, Europhys. Lett. **19**, 699 (1992).
5) I. F. Herbut, Phys. Rev. Lett. **97**, 146401 (2006).
6) M.-T. Tran and K. Kuroki, Phys. Rev. B **79**, 125125 (2009).

7) S. A. Jafari, Eur. Phys. J. B **68**, 537 (2009).
8) Z. Y. Meng, T. C. Lang, S. Wessel, F. F. Assaad, and A. Muramatsu, Nature **464**, 847 (2010).
9) S. Sorella, Y. Otsuka, and S. Yunoki, Sci. Rep. **2**, 992 (2012).
10) F. Assaad and I. F. Herbut, Phys. Rev. X **3**, 031010 (2013).
11) F. Parisen Toldin, M. Hohenadler, F. F. Assaad, and I. F. Herbut, arXiv:1411.2502.
12) C.-C. Chang and R. Scalettar, Phys. Rev. Lett. **109**, 026404 (2012).
13) D. Ixert, F. F. Assaad, and K. P. Schmidt, Phys. Rev. B **90**, 195133 (2014).
14) W. Wu, Y.-H. Chen, H.-S. Tao, N.-H. Tong, and W.-M. Liu, Phys. Rev. B **82**, 245102 (2010).
15) A. Liebsch, Phys. Rev. B **83**, 035113 (2011).
16) A. Liebsch and H. Ishida, J. Phys.: Condens. Matter **24**, 053201 (2012).
17) S.-L. Yu, X. Xie, and J.-X. Li, Phys. Rev. Lett. **107**, 010401 (2011).
18) W. Wu, S. Rachel, W.-M. Liu, and K. Le Hur, Phys. Rev. B **85**, 205102 (2012).
19) R.-Q. He and Z.-Y. Lu, Phys. Rev. B **86**, 045105 (2012).
20) K. Seki and Y. Ohta, arXiv:1209.2101.
21) S. Hassan and D. Sénéchal, Phys. Rev. Lett. **110**, 096402 (2013).
22) A. Liebsch and W. Wu, Phys. Rev. B **87**, 205127 (2013).
23) Q. Chen, G. H. Booth, S. Sharma, G. Knizia, and G. K.-L. Chan, Phys. Rev. B **89**, 165134 (2014).
24) M. Laubach, J. Reuther, R. Thomale, and S. Rachel, Phys. Rev. B **90**, 165136 (2014).
25) Y. Hatsugai, T. Fukui, and H. Aoki, Phys. Rev. B **74**, 205414 (2006).
26) M. Potthoff, M. Aichhorn, and C. Dahnken, Phys. Rev. Lett. **91**, 206402 (2003).
27) D. Sénéchal, arXiv:0806.2690.
28) M. Potthoff, in *Strongly Correlated Systems - Theoretical Methods*, ed. A. Avella and F. Mancini (Springer, Berlin, 2012) Vol. 171, Chap. 10, p. 303.
29) M. Potthoff, Eur. Phys. J. B **32**, 429 (2003).
30) M. Potthoff, Eur. Phys. J. B **36**, 335 (2003).
31) C. Dahnken, M. Aichhorn, W. Hanke, E. Arrigoni, and M. Potthoff, Phys. Rev. B **70**, 245110 (2004).
32) D. Sénéchal, in *Strongly Correlated Systems - Theoretical Methods*, ed. A. Avella and F. Mancini (Springer, Berlin, 2012) Vol. 171, Chap. 11, p. 341.
33) M. Balzer, B. Kyung, D. Sénéchal, A.-M. S. Tremblay, and M. Potthoff, Europhys. Lett. **85**, 17002 (2009).
34) D. Sénéchal, D. Perez, and M. Pioro-Ladrière, Phys. Rev. Lett. **84**, 522 (2000).
35) S. Rachel, M. Laubach, J. Reuther, and R. Thomale, arXiv:1411.4649.